



A DNA damage–induced phosphorylation circuit enhances Mec1^{ATR} Ddc2^{ATRIP} recruitment to Replication Protein A

Luke A. Yates^a , Elias A. Tannous^b , R. Marc Morgan^c , Peter M. Burgers^d, and Xiaodong Zhang^{a,1}

Edited by Lorraine Symington, Columbia University Irving Medical Center, New York, NY; received January 4, 2023; accepted February 24, 2023

The cell cycle checkpoint kinase Mec1^{ATR} and its integral partner Ddc2^{ATRIP} are vital for the DNA damage and replication stress response. Mec1–Ddc2 “senses” single-stranded DNA (ssDNA) by being recruited to the ssDNA binding Replication Protein A (RPA) via Ddc2. In this study, we show that a DNA damage–induced phosphorylation circuit modulates checkpoint recruitment and function. We demonstrate that Ddc2–RPA interactions modulate the association between RPA and ssDNA and that Rfa1-phosphorylation aids in the further recruitment of Mec1–Ddc2. We also uncover an underappreciated role for Ddc2 phosphorylation that enhances its recruitment to RPA–ssDNA that is important for the DNA damage checkpoint in yeast. The crystal structure of a phosphorylated Ddc2 peptide in complex with its RPA interaction domain provides molecular details of how checkpoint recruitment is enhanced, which involves Zn²⁺. Using electron microscopy and structural modeling approaches, we propose that Mec1–Ddc2 complexes can form higher order assemblies with RPA when Ddc2 is phosphorylated. Together, our results provide insight into Mec1 recruitment and suggest that formation of supramolecular complexes of RPA and Mec1–Ddc2, modulated by phosphorylation, would allow for rapid clustering of damage foci to promote checkpoint signaling.

checkpoint kinase | DNA damage signaling | structural biology | protein phosphorylation | replication stress

The cell cycle checkpoint is a signaling pathway that coordinates DNA repair and replication challenges with cell cycle progression to safeguard the genome. The kinase Mec1 (mitosis entry checkpoint), and its human counterpart ATR (Ataxia-Telangiectasia Mutated and Rad3 related), are master regulators of the checkpoint that are crucial for DNA replication, DNA damage, and replication stress responses. Mec1, a member of the phosphatidylinositol 3-kinase like kinase family, is essential in yeast (1, 2), and ATR loss is early embryonic lethal in mammals (3, 4). Mec1/ATR dysfunction increases genomic instability in S-phase and causes chromosomal rearrangements (5, 6). Hypomorphic mutations in human ATR is associated with Seckel syndrome, an autosomal recessive disorder characterized by microcephaly, dwarfism, and intellectual disability (7).

Double-strand breaks occurring in S and G2 phases are repaired by homologous recombination (HR), which utilizes regions of homology in sister chromatids as a template. During HR, the broken DNA ends are resected to produce long 3′ single-stranded DNA (ssDNA) overhangs. Stalled replication forks also produce long and persistent stretches of ssDNA. In both cases, the ssDNA is coated by Replication Protein A (RPA), a ubiquitous ssDNA-binding protein that protects the DNA from degradation, undesired pairing, and secondary structure formation (8). Mec1/ATR is recruited to RPA–ssDNA nucleoprotein filaments via its integral binding partner Ddc2/ATR-interacting protein (ATRIP) (9). Mec1/ATR coordinates cell cycle progression with DNA repair or fork stabilization and a major cellular consequence of its activity is histone H2A phosphorylation (a bona fide signal of DNA damage) and cell cycle arrest via Rad53/CHK1 phosphorylation. Mec1–Ddc2 therefore maintains a low level of kinase activity, which is not increased upon RPA-dependent recruitment, but instead requires cell-cycle-specific activators for proper function (10). We recently uncovered a mechanism for how Mec1–Ddc2 is maintained in an autoinhibited state, and the conformational changes required to transition into an activated state (11). Given that a number of Mec1 activators are associated with chromatin, controlled recruitment of Mec1–Ddc2 by posttranslational modifications (PTMs) could also be a means to regulate its cellular activity (12–14). Autophosphorylation of Mec1 is also important for its function (15, 16) and occurs in trans (13) implying that Mec1–Ddc2 must be brought together for this to occur. The localized Mec1 response at the DNA lesion site, characterized by H2A S129 phosphorylation, is rapid and hypersensitive to low levels of ssDNA (17). Further, Mec1–Ddc2 is anchored at specific locations in damaged chromatin (17), suggesting a DNA damage–induced mechanism for rapid and stable recruitment of Mec1–Ddc2

Significance

The DNA damage and replication stress response protein, Mec1^{ATR}, is recruited to single-stranded DNA via the ubiquitous ssDNA-binding protein, Replication Protein A (RPA). Using a combination of structural, biochemical, biophysical, and genetic approaches, we report a phosphorylation circuit that drives Mec1 recruitment that is important for the DNA damage checkpoint. Our studies uncover a mode of protein oligomerization through phosphorylation, with a role for Zn²⁺ coordination within this assembly. We propose the formation of higher order supramolecular complexes between RPA and Mec1–Ddc2 that is enhanced by phosphorylation as an important mechanism of the DNA damage checkpoint signaling.

Author affiliations: ^aSection of Structural Biology, Department of Infectious Disease, Imperial College London, South Kensington, London SW7 2AZ, United Kingdom; ^bDepartment of Biochemistry and Molecular Biophysics, Washington University School of Medicine, Saint Louis, MO 63110; and ^cDepartment of Life Sciences, Centre for Structural Biology, Imperial College London, South Kensington, London SW7 2AZ, United Kingdom

Preprint Servers: BioRxiv, <https://doi.org/10.1101/2022.12.23.521831>.

Author contributions: L.A.Y., E.A.T., P.M.B., and X.Z. designed research; L.A.Y., E.A.T., and R.M.M. performed research; L.A.Y., E.A.T., P.M.B., and X.Z. analyzed data; and L.A.Y., E.A.T., P.M.B., and X.Z. wrote the paper.

The authors declare no competing interest.

This article is a PNAS Direct Submission.

Copyright © 2023 the Author(s). Published by PNAS. This open access article is distributed under [Creative Commons Attribution License 4.0 \(CC BY\)](https://creativecommons.org/licenses/by/4.0/).

¹To whom correspondence may be addressed. Email: xiaodong.zhang@imperial.ac.uk.

This article contains supporting information online at <https://www.pnas.org/lookup/suppl/doi:10.1073/pnas.2300150120/-DCSupplemental>.

Published March 30, 2023.

to RPA-ssDNA, which we hypothesize relies on posttranslational modifications. However, a detailed molecular understanding of how Mec1–Ddc2 recruitment to RPA-ssDNA could be modulated by PTMs remains unclear.

Yeast RPA consists of three subunits, Rfa1 (RPA70 in human), Rfa2 (RPA32) and Rfa3 (RPA14), with each subunit consisting of one or more ssDNA-binding OB-fold domains (DBDs). The Rfa1/RPA70 N-terminal domain (NTD) is a predominantly protein-interacting module and specifically interacts with Ddc2/ATRIP (18). Previous studies have shown that direct interactions between Rfa1-NTD and the N-terminal region of Ddc2 (19) or ATRIP (20) are essential for checkpoint function. Structural studies of the Mec1–Ddc2, which is a stable dimer of heterodimers (11), together with a complex structure between a homodimeric N-terminal coiled-coil domain of *Kluyveromyces lactis* Ddc2 and *Saccharomyces cerevisiae* Rfa1-NTD (21), suggest a 2:2:2 arrangement of RPA, Mec1, and Ddc2. Further, the N-terminal Ddc2 α -helical acidic domain is engulfed by a positively charged groove of the Rfa1-NTD OB-fold, similar to other Rfa1/RPA70-NTD interacting domains (21, 22). Additionally, RPA interacts with many repair factors through the Rfa1/RPA70-NTD via its positively charged groove, raising questions about how different RPA-interacting DNA damage factors are selectively recruited. Previously, we have shown that *S. cerevisiae* RPA forms oligomers on ssDNA via an inter-RPA interaction between the OB domain of Rfa1 and the OB domain of Rfa3 of an adjacent RPA. Importantly, we have shown that this oligomerization is enhanced using a phosphomimetic substitution at S178 of the Rfa1 subunit (23), which is a Mec1-dependent phosphorylation site (24). However, the precise effect of this phosphorylation on the recruitment of Mec1–Ddc2 and damage foci formation remains unclear.

In this work, we set out to investigate the interactions between RPA and Mec1–Ddc2 and the modulation of kinase recruitment. Our results reveal that Rfa1-S178 phosphorylation enhances Mec1–Ddc2 recruitment, and the binding of Ddc2 dimers in turn enhances RPA clustering. Further, we find that Serine11 phosphorylation in Ddc2 modulates the interactions between Mec1–Ddc2 and RPA and plays a crucial role in Mec1–Ddc2-dependent DNA damage response. Significantly, our studies uncover a mode of protein oligomerization through phosphorylation, with a role for Zn^{2+} binding within this assembly. We propose a recruitment strategy that allows fast accumulation of Mec1–Ddc2 at damaged sites through DNA damage–induced phosphorylation of RPA and Ddc2, stabilized by Zn^{2+} ions, that has the potential to promote damage foci and Mec1 autophosphorylation.

Results

Phosphorylation of RPA at S178 Enhances Mec1–Ddc2 Recruitment. We previously provided a model for how multiple RPAs form higher order structures to coat ssDNA (23). We also showed that mimicking phosphorylation of Rfa1-S178 causes enhanced *trans* RPA–RPA interactions resulting in cooperative ssDNA binding (23, 25). RPA is a major platform for Mec1–Ddc2 recruitment (9, 26, 27), and the removal of RPA from ssDNA via the Srs2 helicase, for example, has been shown to dampen the checkpoint (28). Therefore, we reasoned that the enhanced clustering of RPA via Rfa1 phosphorylation could play a role in checkpoint kinase recruitment. We set out to address this question by characterizing interactions between Mec1–Ddc2 with RPA alone and bound to ssDNA. Previous work has established that the Mec1–Ddc2 complex forms head-to-head dimers of Mec1–Ddc2 heterodimers via several regions, including the Mec1 kinase,

FAT (FRAP, ATM, TRAPP) domains, and Ddc2 C-terminal HEAT (Huntingtin, elongation factor 3, protein phosphatase 2A (PP2A), and TOR1) repeats (Fig. 1A) (11, 29). Further, the N-terminal region of Ddc2 forms a coiled-coil dimer and, importantly, possesses a well-characterized RPA-interaction site (Fig. 1A) (19, 21). Using biotinylated-dT₃₂ oligonucleotide immobilized to streptavidin beads, we were able to show that phosphomimetic RPA^{S178D} (RPA with an Rfa1^{S178D} subunit) binding to purified Mec1–Ddc2 complexes was not grossly perturbed compared with RPA^{WT} (SI Appendix, Fig. S1). Due to the limited quantity of purified Mec1–Ddc2 for biophysical studies, and given that the major RPA-interaction sites are situated at the N terminus of Ddc2, we constructed and purified an N-terminal Ddc2 fragment containing the main RPA-binding site together with the coiled-coil domain (residues 1–148, denoted as Ddc2–CC, Fig. 1A and B), which should maintain a dimeric state. Indeed, Ddc2–CC domains are dimers, confirmed using size exclusion chromatography multi angle light scattering (SEC-MALS), and are able to interact with RPA, measured by microscale thermophoresis (MST) (SI Appendix, Fig. S2A and B). Using this Ddc2–CC fragment, we assessed its binding to RPA-coated ssDNA using MST. Ddc2–CC binds to RPA-dT₁₀₀ nucleoprotein with similar affinity to RPA alone (Fig. 1B and SI Appendix, Fig. S2C). RPA^{S178D} showed an improved

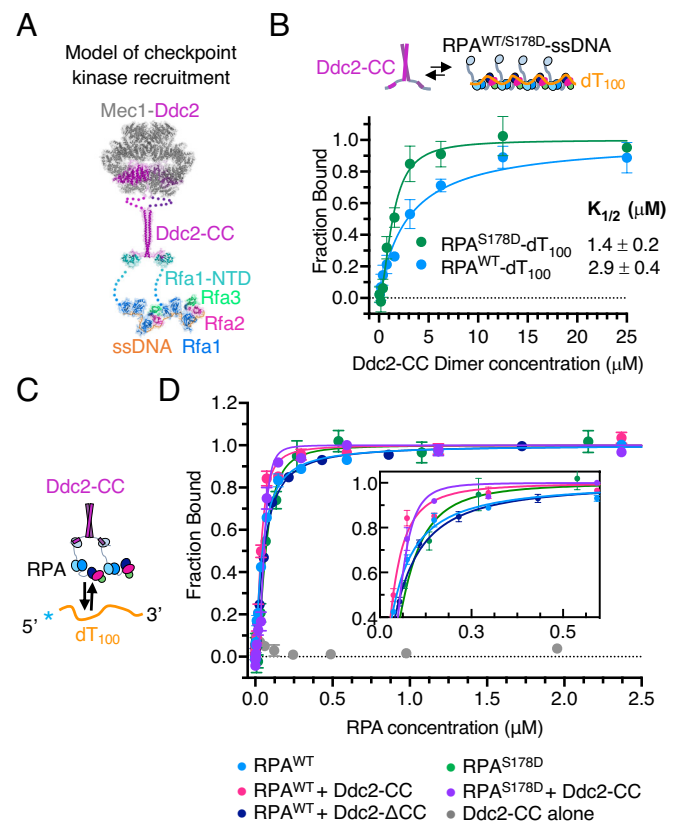


Fig. 1. Interaction studies between Mec1–Ddc2 and RPA. (A) Model of Mec1–Ddc2 recruited by RPA-ssDNA based upon available structural data (11, 21, 23). (B) MST-binding curves of Ddc2–CC versus RPA^{WT} or phosphomimetic mutant RPA (RPA^{S178D}) bound to homopolymer ssDNA (dT₁₀₀). (C) Schematic of Ddc2–CC dimers tethering RPA to influence its association with ssDNA. (D) MST-binding curves of RPA complexes interacting with Cy5-labeled dT₁₀₀ ssDNA substrate, using RPA^{WT} or RPA^{S178D}, in the absence or presence of Ddc2–CC. For all MST data the normalized fluorescence was analyzed using NanoTemper Analysis 1.2.101 and expressed as fraction bound. Measurements were repeated at least 3 times or more and data points are averages with standard error (SE). The concentration at which half is bound (K_{1/2}) are similar with increased rate of saturation when Ddc2–CC is present, suggestive of RPA tethering by Ddc2–CC.

affinity (twofold) for the Ddc2–CC fragment (Fig. 1B), suggesting that Rfa1^{S178} phosphorylation enhances Ddc2 interactions, and by extension Mec1–Ddc2 recruitment, which supports yeast coimmunoprecipitation experiments with RPA-S178A that show a 50% reduced Mec1 recruitment capacity (30).

We next tested whether Ddc2–CC:RPA complexes alter the behavior of RPA nucleoprotein filament assembly. To quantify these interactions, we used MST to measure direct binding between RPA and ssDNA in the absence and presence of Ddc2–CC. The addition of Ddc2–CC does not affect the interaction between RPA and ssDNA (Fig. 1D). This is not surprising, as Ddc2–CC does not bind to ssDNA (Fig. 1D) but interacts with Rfa1-NTD, which is independent of the DNA-binding domains (31). However, the tethering of RPAs via the homodimeric Ddc2 fragment causes ssDNA binding by RPA to become cooperative, as suggested by the binding curves, but not when the coiled-coil region is removed (Fig. 1D). This cooperativity is further enhanced when combined with the RPA^{S178D} mutant, suggesting an additive effect due to two independent mechanisms coupling RPA molecules together. Additional experiments using electrophoretic mobility shift assays show improved RPA coating in the presence of Ddc2–CC, consistent with MST data (SI Appendix, Fig. S2D).

RPA–ssDNA can also loop during replication (32), or during end-resection (33), which may influence Mec1–Ddc2 recruitment. We next probed if Ddc2–CC, and by extension Mec1–Ddc2, can also bridge two separate RPA-coated ssDNA molecules (SI Appendix, Fig. S2E and F). We designed a pull-down assay to capture a second RPA–ssDNA molecule, carrying a fluorophore, with an immobilized RPA–ssDNA in the presence or absence of Ddc2–CC. In the absence of Ddc2–CC, we found that RPA–ssDNA could also capture a second RPA–ssDNA molecule, presumably due to the dynamic behavior of RPA DBDs (23). However, there was a significant increase in RPA (Ddc2–CC is not detected in this assay) and Cy5–ssDNA captured when Ddc2–CC was present, suggesting Ddc2–CC could bind to two separate stretches of RPA–ssDNA. RPA^{S178D} did not show significant differences compared with RPA. These data suggest that Mec1–Ddc2 can bind across two separate regions of RPA–ssDNA that are not necessarily close in space and this binding does not depend on S178 phosphorylation.

Collectively, these data show that *trans* RPA–RPA interactions that promote clustering are important for the recruitment of Mec1–Ddc2 complexes. In addition, the tethering of RPA via its interaction with dimeric Ddc2 promotes cooperative binding to ssDNA. Mec1–Ddc2 could possibly bind to distal regions of RPA–ssDNA. This synergistic enhancement results in more stably recruited Mec1–Ddc2 complexes and infers a feed-forward loop involving phosphorylation of Rfa1, which is predominantly Mec1 dependent (24), in recruiting and retaining checkpoint kinase at ssDNA.

Phosphorylation of the Ddc2 N Terminus Enhances Association with RPA. Since Rfa1-S178 phosphorylation influences Mec1–Ddc2 association, we next asked if phosphorylation of Mec1–Ddc2 can also influence recruitment. Proteomic and genetic studies have demonstrated a number of phosphorylation sites in Mec1–Ddc2 that are important for function (13, 34). We found that purified Mec1–Ddc2 used in our previous studies is extensively phosphorylated, and the majority of Ddc2's phosphorylation can be removed by phosphatase treatment (SI Appendix, Fig. S3A). The Mec1 phosphosites previously described (13) are not easily accessible to phosphatase treatment, and we suspect that these are buried in this functional state. This prompted us to investigate

the role of Mec1–Ddc2 phosphorylation on RPA–ssDNA interaction. We purified Mec1–Ddc2 complexes in which Ddc2 harbored a FLAG-tag at the N terminus (a kind gift of J. Diffley) (SI Appendix, Fig. S3B) and labeled it with a fluorescent (Alexa Fluor-647) anti-FLAG antibody. During the Mec1–Ddc2 purification, we carefully preserved the phosphorylation status by including phosphatase inhibitors at every step. Finally, we separated the Mec1–Ddc2 samples into two aliquots; one treated with lambda-phosphatase, and the other with reaction buffers only, resulting in phosphorylated or dephosphorylated samples (Fig. 2A). MST-binding results using a titration of RPA–dT₁₀₀ nucleoprotein complexes produced a dissociation constant of 0.7 μ M for phosphorylated Mec1–Ddc2 (Fig. 2B). Dephosphorylated Mec1–Ddc2 produced a K_d of 4.1 μ M (Fig. 2B), ~sixfold weaker than phosphorylated samples but is similar to the K_d obtained for unmodified Ddc2–CC (SI Appendix, Fig. S2C). These data suggest that phosphorylation of Mec1–Ddc2 (most likely Ddc2) enhances binding to RPA–ssDNA.

To identify potential phosphorylation sites responsible for the enhanced binding to RPA, we focused on those phosphosites previously described in Ddc2 that are close to the known RPA interaction sites—a motif that is often identified by a negatively charged Asp-rich region (35). Proteomic studies have identified two Ddc2 phosphorylation sites, Serine10 and Serine11, adjacent to the highly conserved RPA-interacting motif (36–38) (Fig. 2C). Both Serine10 and Serine11 phosphorylation have been robustly detected when cells are exposed to methylmethane sulfonate (39). These two phosphosites are also conserved in other species but are often found to be substituted by aspartate, particularly at the equivalent S11 site, suggesting natural phosphomimetics (Fig. 2C). We thus introduced substitutions into Ddc2 to mimic states that are constitutively phosphorylated (Ser to Asp) or unphosphorylated (Ser to Ala) and tested their effects on growth and sensitivity to replication inhibitor hydroxyurea (HU) or ultraviolet light (UV) damage in several indicator strains that are progressively compromised for the cell cycle checkpoint circuitry (Fig. 2D and SI Appendix, Fig. S4A). Ddc2-S10A, Ddc2-S10D, and Ddc2-S11D phenocopy wild type (WT) yeast under the conditions tested (Fig. 2D). On the other hand, S11A shows growth defects and is very sensitive to HU, but limited UV sensitivity (Fig. 2D). This sensitivity was also phenocopied by a S10A–S11A double mutant, whereas S10D–S11D mutants are analogous to WT (SI Appendix, Fig. S4A), suggesting nonphosphorylatable S11 compromises Ddc2 function in replication stress. Kinase activity of purified Mec1–Ddc2(S10D/A) and Mec1–Ddc2(S11D/A) mutants were not obviously compromised, suggesting the checkpoint-defective phenotypes observed are related to recruitment deficiencies in yeast (SI Appendix, Fig. S4B). We therefore predicted that both S10 and S11 phosphosites in Ddc2 could modulate the association with RPA, given their close proximity to the known interaction motif. To this end, we tested the relative affinities between synthetic phosphorylated and unmodified Ddc2 peptides (amino acids 4 to 24) with Rfa1-NTD (residues 1 to 132) using isothermal titration calorimetry (ITC) (Fig. 2E and F and SI Appendix, Fig. S4C). ITC isotherms show that the unmodified Ddc2 peptide (denoted WT) binds to Rfa1-NTD with an ~2 μ M dissociation constant (K_D) (Fig. 2F). Phosphorylation of either Serine10 (pS10) or Serine11 (pS11) produced approximately threefold and sevenfold improved affinity, respectively (Fig. 2F). A bis-phosphorylated peptide (pS10–pS11) showed a similar affinity to pS11-peptide, suggesting S11 plays a dominant role (SI Appendix, Fig. S4C). Interestingly, the fold increase in affinity observed for S11 phosphorylation is similar to that observed between phosphorylated

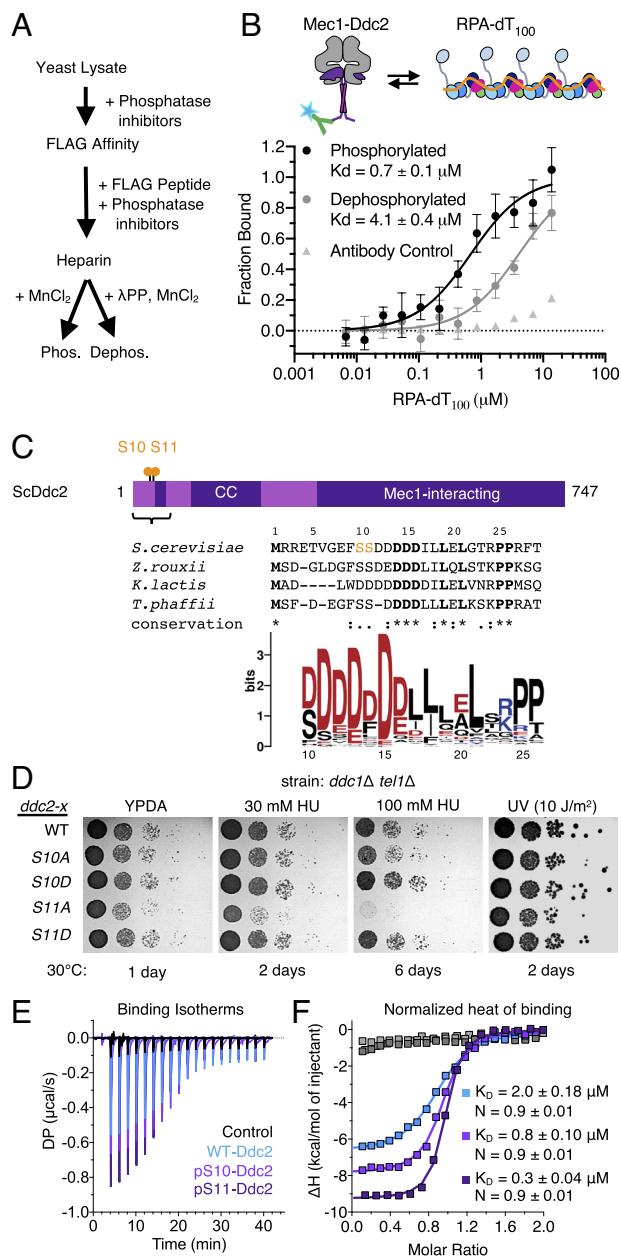


Fig. 2. Phosphorylation of Ddc2 enhances recruitment to RPA and is important for the damage response. (A) Purification strategy for comparing phosphorylated and dephosphorylated (treated with λ-protein phosphatase, λPP) Mec1–Ddc2 by MST. (B) MST binding curves using Mec1–Ddc2 or Mec1–Ddc2 treated with lambda-phosphatase versus RPA-ssDNA. Approximately 100 nM Mec1–Ddc2 complex was mixed with equimolar amounts of Alexa Fluor 647-conjugated anti-FLAG antibody to label the Ddc2 subunit, which harbors an N-terminal 3×FLAG tag, and used for MST versus a serial dilution of RPA-ssDNA at concentrations indicated. Antibody alone was used as a control. Fraction bound was estimated using the averaged normalized fluorescence and fitting the data using a law of mass action equation in Nanotemper analysis software. (C) Schematic of domains in Ddc2 along with its phosphorylation sites. S10 and S11, the focus of this study, are shown by orange circles. A sequence alignment of the RPA-interacting region from other yeast species is shown underneath. An amino acid frequency plot from alignment of 90 Ddc2 sequences from different fungi species showing a high conservation of acidic residues. Numbering underneath corresponds to *S. cerevisiae* Ddc2 numbering. (D) Growth of *DDC2* mutants. Strain PY437 is *ddc2Δ tel1Δ ddc1Δ* and contain plasmid *p(LEU2 ddc2-x)*. The strain was tested for growth on yeast extract peptone dextrose adenine (YPDA) plates with or without hydroxyurea (HU) or treatment with ultraviolet light (UV) as indicated. (E) Raw isothermal titration calorimetry and (F) normalized heat of binding isotherms (Lower) for Ddc2 peptides and phosphorylation variants titrated against Rfa1-NTD (purple) or buffer alone (heat of dilution controls, gray/black). Calculated dissociation constants (K_D) are derived from the measured association constant by linear regression fitting using a 1-to-1 binding model in MicroCal PEAQ-ITC analysis software.

and dephosphorylated Mec1–Ddc2 binding to RPA-ssDNA. This is consistent with the idea that phosphorylation of Ddc2 could be responsible for the enhanced binding between Mec1–Ddc2 and RPA-ssDNA. Our genetic studies along with our interaction studies show that S11 is more important for function in vivo, consistent with ITC data that S11 phosphorylation has a larger effect on binding (Fig. 2 F and G).

Structure of Rfa1-NTD in Complex with a Phosphorylated Ddc2 Peptide. To understand the molecular basis of the phosphorylation events and how it might affect the binding, we determined a crystal structure of *Sc*Rfa1-NTD in complex with a phosphorylated *Sc*Ddc2 peptide (residues 4 to 24) to 1.58 Å resolution (Fig. 3A and Table 1 and *SI Appendix, Fig. S5 A–C*). The structure was solved by molecular replacement using the Rfa1-NTD structure from Protein Data Bank (PDB:5OMB) as a search model. We were able to clearly resolve the majority of the Ddc2 peptide (residues 10 to 24), including the pS11 (Fig. 3A). However, residues 4 to 9 were invisible due to flexibility and that they do not interact with the Rfa1-NTD. Overall, the Ddc2 peptide interacts in similar way to the *K. lactis* Ddc2 with *Sc*Rfa1-NTD (*SI Appendix, Fig. S5 D and E*).

Critically, Asp12 and Asp13, together with phosphoserine11, coordinate two metal ions in the structure. The electron density from an omit map showed clear positive difference density for metal ions (Fig. 3B). Given that the crystallization conditions contain ZnCl₂, we postulate the metal ions to be Zn²⁺. Indeed, peptides that are aspartate-rich have been shown to bind to zinc ions (40), and in the structure, the ions are tetrahedrally coordinated by carboxyl groups of the aspartate side chains, oxygen groups of the phosphoserine, and water molecules (Fig. 3B). The coordination geometry and bond lengths are consistent with zinc binding (~2.0 Å in the structure) and were supported by using the CMM metal-binding site validation server (42). We further confirmed the pS11–Ddc2 peptide’s ability to coordinate zinc and no other divalent cations (magnesium or calcium) by ITC (Fig. 3C and *SI Appendix, Fig. S6 B–D*). Clear binding was observed when ZnCl₂ was titrated against the pS11–Ddc2 peptide, but not for either CaCl₂ or MgCl₂ (*SI Appendix, Fig. S6 B–D*). To validate the zinc coordination observed in our structure, we performed additional ITC-binding experiments using Ddc2 peptide variants. Our ITC data show that when a zinc coordination donor is removed, i.e. unphosphorylated, D12A, or D13A, the apparent affinity decreases ~twofold compared with pS11–Ddc2 peptide (Fig. 3 C and D and *SI Appendix, Fig. S6 E–H*). A double D12A/D13A substitution reduces the phosphopeptide affinity for zinc by ~tenfold (Fig. 3 C and D). The importance of D12–D13 is underscored by its conservation in yeasts and humans, and is supported by biochemical and genetic studies, which show that D12K and D13K substitutions in Ddc2 results in defective RPA–Ddc2 interactions (19). To further probe the Rfa1-NTD–pS11-peptide complex and zinc binding, we performed MST, which show comparable pS11 peptide–Zn²⁺ affinities to that obtained by ITC. The relative affinity for zinc increases when the pS11 peptide is in complex with Rfa1-NTD and does not bind a range of other metals (*SI Appendix, Fig. S7 A and B*). The zinc ion coordination in our structure is unusual, with phosphoserine and aspartate residues infrequently observed in zinc coordination sites in the protein data bank (42). Generally structural zinc-coordination spheres are comprised predominantly of cysteine and histidine residues and possess nM–pM affinities for zinc (42), with both Rfa1 and Mec1 possessing such zinc sites (11, 23). The zinc coordination and the weak/moderate affinities measured, suggests that these metal ions are not likely to serve a structural role. Instead, pS11–Ddc2 may bind zinc with fluctuating metal concentrations in yeast; for example, during increased oxidative stress or when zinc is in excess.

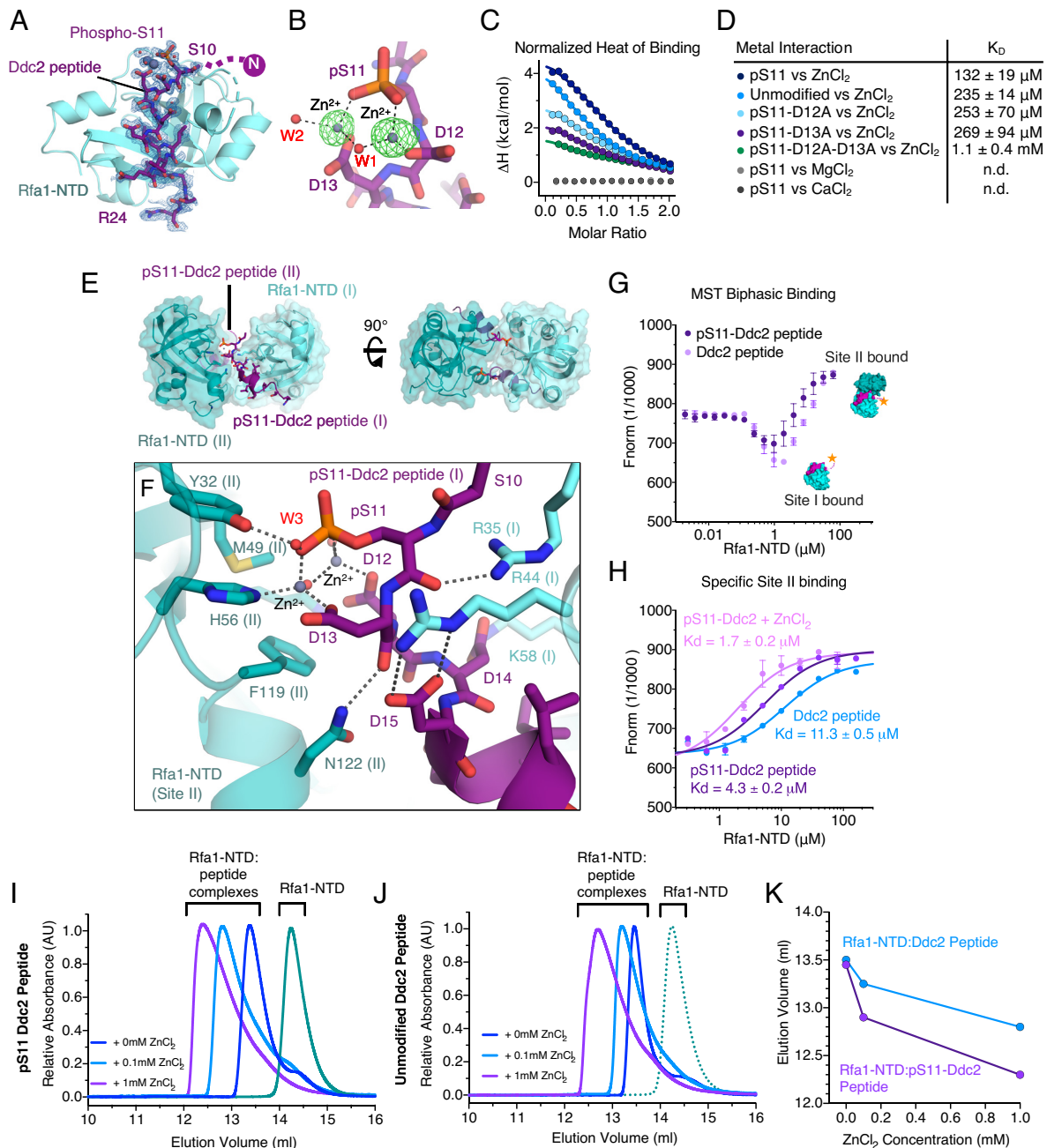


Fig. 3. Structural basis for Rfa1-NTD dimer assembly via pS11-Ddc2 binding. (A) Crystal structure of Rfa1-NTD:pS11-Ddc2 peptide complex refined to 1.58 Å resolution. Rfa1-NTD is displayed as ribbon and rendered pale blue. Bound pS11-Ddc2 peptide is shown as sticks and rendered in purple. Heteroatoms are also colored (red, oxygen; nitrogen, blue). Ordered waters and metal ions (Zn^{2+}) are shown as red and gray spheres, respectively. Feature enhanced map electron density, calculated in PHENIX, is shown as blue mesh (1 sigma) and carved around the peptide and metals (at 1.8 Å). (B) Molecular details of Ddc2 peptide phosphoserine11 (pS11) coordinating two zinc ions (gray spheres), with waters (red spheres) and Ddc2 residues D12 and D13 with a simulated annealing omit map (Fo-Fc) of coordinated metal ions (green mesh, contoured to 10 sigma). (C and D) ITC isotherm-binding curves from metals titrated against pS11-Ddc2 and variants removing coordination donors. The binding affinity for Zn^{2+} decreases along with the heat of binding (ΔH , kcal/mol) when a zinc coordination donor is removed by substitution, with unphosphorylated, D12A, and D13A showing both a reduced affinity and heat of binding when compared with pS11-Ddc2 peptide. A double-mutant D12A-D13A shows significantly diminished binding. Neither calcium nor magnesium show any detectable binding. Calculated dissociation constants (K_D) are provided in D. (E) Orthogonal views of the Rfa1-NTD:pS11-Ddc2 complex dimer arrangement in the crystal lattice. (F) Molecular details of the pS11-Ddc2 binding interface on the second Rfa1-NTD molecule. (G) Biphasic MST binding curves of 6-FAM-labeled Ddc2 peptides versus Rfa1-NTD. (H) MST binding curves focusing on the secondary site, which occurs at Rfa1-NTD concentrations above site I saturation, with unmodified or S11 phosphorylated Ddc2 peptides and with 1 mM $ZnCl_2$. To obtain a K_d value, MST curves were fitted with the law of mass action equation in Nanotemper analysis software. (I–K) size exclusion chromatography (SEC) of Rfa1-NTD in complex with pS11-Ddc2 or unmodified Ddc2 peptides and separated on a Superdex S75 (10/300) in buffer containing 0 mM, 0.1 mM and 1 mM $ZnCl_2$. (K) SEC peak elution volumes are plotted as a function of zinc concentrations.

Ddc2 Phosphorylation Promotes Oligomerization of RPA. In the crystal lattice, we observe that the Ddc2 (pS11–D12–D13): Zn^{2+} coordinated complex, which protrudes from the Rfa1-NTD, contacts another Rfa1-NTD that completes the tetrahedral coordination of one of the zinc ions via H56 of the second Rfa1-NTD molecule (Fig. 3 E and F). This arrangement is reciprocated

by the second Rfa1-NTD molecule forming a “fireman’s grip” that maintains a 1:1 stoichiometry (Fig. 3E), consistent with our ITC. Further, this second Rfa1-NTD (denoted a Rfa1-NTD’) contributes to the Ddc2 peptide binding via residues Y32, H56, and N122 (Fig. 3F). Specifically, Y32 contacts pS11 via a water molecule (Fig. 3F). The zinc ions are coordinated by Rfa1-NTD’-H56,

Table 1. Crystallographic data collection and refinement statistics

	Rfa1-NTD:pS11-Ddc2 complex (PDB 8B4J)	Rfa1-NTD (PDB 8B4K)
Data collection		
Wavelength (Å)	0.979	0.979
Space group	P 6 ₅ 2 2	P 2 ₁
Cell dimensions		
<i>a</i> , <i>b</i> , <i>c</i> (Å)	40.0, 40.0, 282.1	54.5, 34.6, 99.4
α , β , γ (°)	90.0, 90.0, 129.0	90.0, 90.1, 90.0
Resolution (Å) [§]	56.4 to 1.58 (1.64 to 1.58)	54.5 to 1.55 (1.61 to 1.55)
Molecules per ASU	1	3
Total no. of reflections	243,031	373,506
No. of unique reflections	19,852 (1,878)	54,483 (5,391)
Completeness (%)	100 (99.3)	99.6 (98.9)
Multiplicity	6.8	6.9
[I/ σ (I)]	23.8 (3.8)	19.8 (3.9)
R _{merge}	0.051 (0.492)	0.039 (0.292)
Refinement		
Resolution (Å)	1.58	1.55
No. of reflections	19,673 (1,878)	54,274 (5,330)
R _{work} /R _{free} (%)	19.1/22.9	16.8/19.0
No atoms		
Protein	2,175	5,716
Zn ²⁺	3	-
Water	72	214
Average B-factors (Å ²)		
Protein	34.89	36.19
Zn ²⁺	25.68	-
Water	39.66	41.92
rmsd		
Bond lengths (Å)	0.01	0.01
Bond angles (°)	1.62	1.37
Ramachandran statistics (%)		
Favored	98.48	99.45
Allowed	1.52	0.55
Outliers	0	0

[§]Values in parentheses are for highest-resolution shell.

Ddc2–D13, and Ddc2–pS11, and are also stabilized by Rfa1-NTD–F119 via cation– π interactions (Fig. 3F). Consistent with measured cation– π interactions, the distance between the F119' ring center and the two zinc ions is 4.5 Å and 5.3 Å, with an angle of approach (θ) of 30.8° and 10.3°, respectively (SI Appendix, Fig. S7C). N122 also contacts the peptide backbone of Ddc2–D13. Structural analysis of this secondary interface by PISA (43) suggests that it is stable in solution. We investigated this secondary site by MST using fluorescently labeled Ddc2 peptides and titrating Rfa1-NTD. This experimental set-up produces a biphasic binding curve by MST, indicating Ddc2 has a high-affinity and a low-affinity Rfa1-interaction site (Fig. 3G). The first phase of binding occurs

in the nanomolar to micromolar range, consistent with our ITC experiments, and the second phase in the micromolar range, which we attribute to the secondary binding site on Rfa1-NTD after the first site is saturated (Fig. 3G). Focused binding studies at Rfa1-NTD concentrations that have saturated the high-affinity site, we find that S11 phosphorylation enhances this interaction threefold (Fig. 3H). The addition of zinc increases the affinity of Ddc2 for the secondary Rfa1-NTD further (~sevenfold) compared with the unmodified peptide (Fig. 3H). This is consistent with our crystal structure, but also suggests that zinc is not obligatory for this interaction. We further investigated Rfa1-NTD dimer formation in solution by pS11-Ddc2 and zinc. We assessed the oligomeric state of Rfa1-NTD:pS11-Ddc2 peptide complexes using analytical size exclusion chromatography (Fig. 3I–K). Our data showed that Rfa1-NTD exists as monomers and when in complex with Ddc2 peptide, a peak shift is observed that is dependent on increasing concentrations of ZnCl₂, which is more pronounced for pS11 peptide (Fig. 3I–K). Cross-linking experiments provide further evidence for oligomerization upon adding pS11 phosphopeptide and ZnCl₂ and match the observations by SEC (SI Appendix, Fig. S8A). Molecular weight estimations by SEC-MALS of Rfa1-NTD:pS11-Ddc2 peptide complex with ZnCl₂ suggests a dimeric species compared to Rfa1-NTD alone (SI Appendix, Fig. S8B). However, the broad peak suggests an equilibrium of dimers and monomers presumably caused by dilution effects during chromatography. The phosphorylation and zinc-enhanced dimerization of RPA also promotes RPA clustering on ssDNA as shown by MST experiments of RPA binding to ssDNA. The presence of pS11-Ddc2 peptide, without the coiled-coil domain, increases the cooperative nature of RPA binding to ssDNA, and this is further increased to 1.8 when zinc is added (SI Appendix, Fig. S8C–F). These data are consistent with the idea that intra-RPA interactions, either via Rfa1-Rfa3 enhanced via Rfa1-S178 phosphorylation, binding to Ddc2-dimers, or phosphorylated Ddc2 (at S11) with zinc, promote cooperative clustering of RPA complexes on ssDNA.

Given the aspartate-rich nature of Ddc2 N terminus, we considered acidophilic kinases that could target this motif—with casein kinase II (CK2), which has the consensus motif S/T-X-X-D/E, being a plausible candidate. An analogous motif is found in *Schizosaccharomyces pombe* topoisomerase II and has been shown to be a bona fide CK2 site (44) (SI Appendix, Fig. S9A). In vitro, we find that Ddc2–CC is a target of recombinant CK2, with two phosphorylation events observed upon kinase treatment (SI Appendix, Fig. S9B and C). Substitution of both S10 and S11 to alanine, but not individual serine substitutions, prevents phosphorylation (SI Appendix, Fig. S10D). We thus used CK2 as a tool to investigate Ddc2-phosphorylation in vitro. Consistent with our peptide studies, phosphorylated Ddc2–CC, via CK2-treatment, shows a significant enhancement in binding to RPA compared with unphosphorylated protein (SI Appendix, Fig. S9E). Further, size exclusion chromatography analysis shows higher order oligomers of phosphorylated Ddc2–CC in complex with Rfa1-NTD upon addition of zinc (SI Appendix, Fig. S9F and G). Superposing available structures, a multivalent arrangement of Rfa1-NTD:Ddc2-CC can be proposed, whereby the dimeric assembly of Rfa1-NTD:pS11-Ddc2 brings together and bridges two Ddc2–CC (thus Mec1–Ddc2) complexes (SI Appendix, Fig. S10). Ddc2–CC complexes, associated to RPA coated on long ssDNAs (~5.3kb) are more resistant to destabilization to high salt when CK2-treated and stabilized by zinc (SI Appendix, Fig. S11). To further investigate the potential higher order assembly, we visualized Mec1–Ddc2 with Rfa1-NTD using negative stain electron microscopy (NSEM). In images of Mec1–Ddc2 in the presence of Rfa1-NTD with and without ZnCl₂, we observe individual complex particles, which are normally a dimer of heterodimers (11), as

well as clusters of higher order complexes, such as dimers of Mec1–Ddc2 heterotetramers, or particles that are closely associated (~50 to 100 Å), which we interpret to be tethered as this distance is approximately the length of Ddc2-CC (Fig. 4A and B). Higher order species are not observed in samples of Mec1–Ddc2 alone (11, 45) nor in Mec1–Ddc2 with ZnCl₂ (Fig. 4C). We used 2D classification to distinguish Mec1–Ddc2 particles that are consistently associated, which persist in 2D class averages, versus those that are randomly close which are averaged away (Fig. 4B and *SI Appendix*, Fig. S12 and *Supplementary Methods*). We observe that the addition of Rfa1-NTD produces a population of Mec1–Ddc2 complex dimers (~14% of total particles) and tethered complexes (~12% of total particles), which are absent in the Mec1–Ddc2 control (Fig. 4C and *SI Appendix*, Fig. S12). The addition of zinc to Mec1–Ddc2 with Rfa1-NTD did not affect the dimer population (~14%) but increased the population of tethered Mec1–Ddc2 complexes to ~26% (Fig. 4C). Overall, the binding of Rfa1-NTD and zinc combined promoted higher order Mec1–Ddc2 assemblies (~40%) compared with Rfa1-NTD alone (~26%) or zinc alone (0%). Using the recent advances in structure prediction by AlphaFold (46) in a Colab AlphaFold multimer implementation (47) to “fill-in” the missing coiled-coil (CC) and N-terminal portion of Ddc2 in our previously determined structure (11), we produced a hybrid model of Mec1–Ddc2 in complex with the Rfa1-NTD (Fig. 5A), which suggests that the kinase domains could face RPA, a known substrate, with the flexible linker allowing a range motion of the kinase. Combining these models with the Rfa1-NTD-Ddc2 dimer induced by phosphorylation, a supramolecular complex of two Mec1–Ddc2 molecules could form (Fig. 5B), consistent with the observations in Fig. 4A. Interestingly, several proteins involved in non-homologous end joining are shown to act as bridges to bring two DNA-PK together (*SI Appendix*, Fig. S10) (48), and are reminiscent of the higher order assemblies observed here.

Discussion

Our study here combines biochemical, biophysical, crystallographic, and yeast genetic studies, collectively supports a model where phosphorylation of RPA (Rfa1-S178) and Ddc2 (S11) promote the clustering of RPA on ssDNA and allow for further oligomerization of Ddc2 via Rfa1-NTD. In turn, the oligomeric state of Mec1–Ddc2 acts to aid RPA clustering on ssDNA by

tethering RPA complexes, and potentially enhancing recruitment efficiency. Specifically, our data show that RPA clustering stimulates Mec1–Ddc2 recruitment, which could lead to the phosphorylation of Rfa1 at S178 by Mec1 (30). The phosphorylation of S178 promotes RPA clustering, amplifies the recruitment of Mec1–Ddc2, and is consistent with Rfa1-S178A mutant RPA that has impaired Mec1 recruitment (30). Reciprocally, dimeric Ddc2 binding to RPA further enhances clustering of RPA through tethering. Studies on ATR have shown that localized crowding of ATR-ATRIP at the replication fork is important for the replication stress response (49) and the exchange of ATR-ATRIP at sites of RPA-coated ssDNA is critical for proper repair in murine models (50). The enhanced RPA clustering via phosphorylation of Rfa1-S178 and interactions with Ddc2, which are further promoted by Ddc2 (S11) phosphorylation and zinc binding, creates a multifaceted, intercalated, and cooperative interaction network that can promote rapid accumulation (or removal) of Mec1–Ddc2. Mec1 recruitment dynamics may be an important aspect of regulating the checkpoint, particularly as the removal of RPA and Mec1–Ddc2 via Srs2 reduces Mec1-signaling (28).

Our study also demonstrates that phosphorylation of Ddc2, particularly at Serine11, enhances binding of Ddc2 to RPA. In vivo and in vitro studies performed here show that phosphorylation of Ddc2-S11 is important for the Mec1-checkpoint, but not its intrinsic kinase activity, consistent with its recruitment role. The structural and biophysical data suggest that Ddc2 phosphorylation of S11 stabilizes Ddc2–RPA complexes through dimerization of Rfa1-NTD, either via “intramolecular” interactions that are derived from the same Ddc2 dimer, but also intermolecular Rfa1-NTD dimerization that acts to promote clustering, both of which being further stabilized by Zn²⁺. In either case, the structural arrangement observed here increases the overall binding surface area and strengthens the interaction. In fact, immunoprecipitation experiments suggest that the RPA-interaction domain containing the N-terminal region of Ddc2 (residues 1 to 57) and lacking the dimeric CC domain promotes homodimerization of Ddc2 under DNA damaging conditions (21). In light of our structural and biophysical data, this could be interpreted as Ddc2 dimerization via Rfa1, in a phosphorylation-dependent manner. This may be important for localizing Mec1–Ddc2 at short stretches of ssDNA where fewer number of RPA molecules are present. Greater numbers of RPA

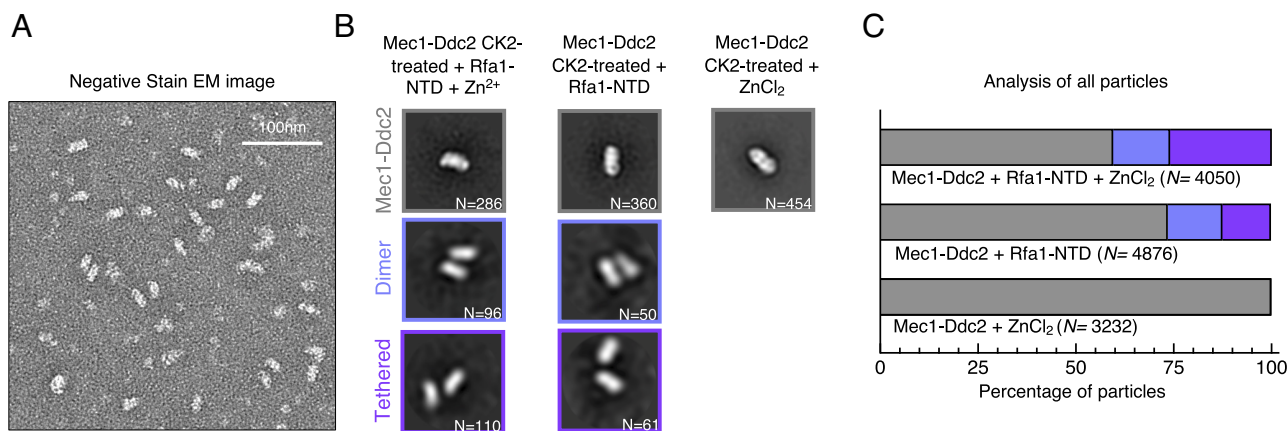


Fig. 4. Electron microscopy of Mec1–Ddc2 complexes. (A) Representative NSEM image of Mec1–Ddc2 in the presence of Rfa1-NTD and 0.1 mM ZnCl₂. (B and C) 2-dimensional (2D) classification analysis using RELION of three NSEM datasets for samples; Mec1–Ddc2 + Rfa1-NTD + 0.1 mM ZnCl₂; Mec1–Ddc2 + Rfa1-NTD; Mec1–Ddc2 + 0.1 mM ZnCl₂ (control). Particles that are close to one another by chance are averaged away in 2D classes, whereas particles consistently associated in high-order assemblies persist in 2D class averages (*SI Appendix*, Fig. S12 and *Supplementary Methods*). Mec1–Ddc2 were pretreated with CK2, which phosphorylates Ddc2 S10511 in vitro. (B) Example 2D class averages of Mec1–Ddc2 particles, which are heterotetramers (denoted Mec1–Ddc2, boxed gray), Mec1–Ddc2 complexes that are in very close contact (denoted Dimer, boxed blue), and closely associated Mec1–Ddc2 complexes within a distance of ~50 to 100 Å (denoted Tethered, boxed purple). The number of particles (N) contributed to each example class is provided (*Inset*). (C) The number of particles associated with each type of class is plotted as a percentage of the total particles analyzed (N) for each dataset.

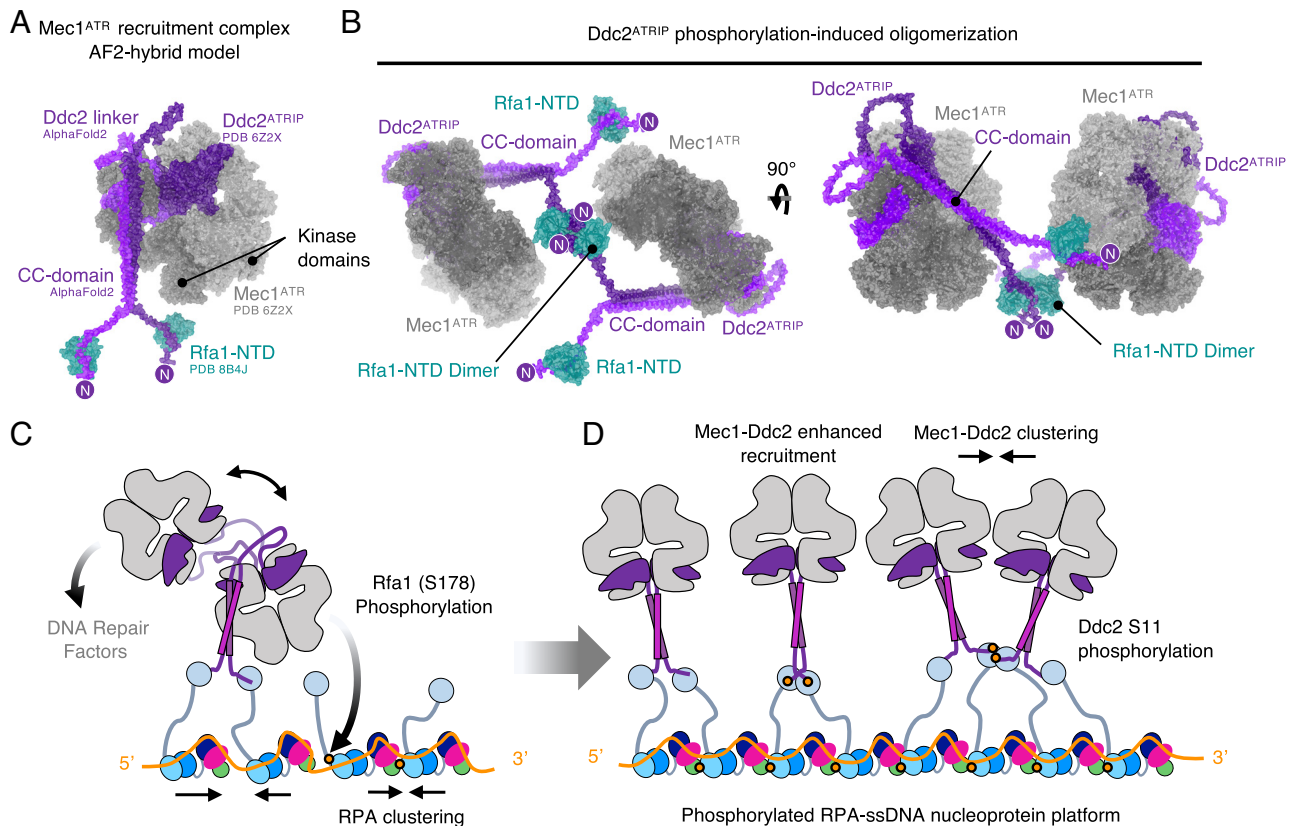


Fig. 5. Model of Mec1–Ddc2 recruitment to RPA-coated ssDNA. (A) Hybrid atomic model of Mec1–Ddc2 in complex with Rfa1-NTD was generated from AlphaFold multimer predictions and experimentally determined structures of Mec1–Ddc2 complex (PDB 6Z2X) and Rfa1-NTD:pS11–Ddc2 peptide (determined in this study, PDB 8B4J). The Mec1 dimer is shown in shades of gray, and the Ddc2-dimer shown in shades of purple and the N terminus of Ddc2 is highlighted. The Rfa1-NTD is colored teal. (B) Orthogonal views of a supramolecular assembly of Mec1–Ddc2 complexes clustered through Rfa1-NTD:pS11–Ddc2 dimerization seen in our crystal structure. (C and D) A model for the phosphorylation circuit driving Mec1–Ddc2 recruitment and clustering proposed from this study. (D) Upon Ddc2 S11 phosphorylation, intramolecular dimerization of Ddc2–RPA interactions enhance recruitment, whereas intermolecular dimerization of Ddc2–RPA interactions aid the clustering of Mec1–Ddc2 complexes.

coating long ssDNA can clearly promote Chk1 phosphorylation by ATR-ATRIP (20), consistent with the model proposed here for RPA clustering and enhanced Mec1–Ddc2 recruitment, which could promote DDR foci formation. The flexible linker in Ddc2 would also allow a range of motion to enable Mec1 to phosphorylate many substrates, or other Mec1–Ddc2 complexes in our multivalent assembly. This arrangement will also likely promote Mec1 auto-phosphorylation, which occurs *in trans*, and is shown to be important for Mec1 function and repair efficiency (13, 15, 16) (Fig. 5D).

The role that zinc plays in the recruitment of Mec1 checkpoint kinase *in vivo* is less clear. In this study, we find that pS11–Ddc2 and the Rfa1-NTD:pS11–Ddc2 complex can specifically bind zinc ions over other metal ions, albeit with moderate/weak affinity. The presence of ZnCl₂ improves complex formation of pS11–Ddc2:Rfa1-NTD, with the crystal structure only obtained when zinc was present. There are multiple examples of zinc ions at protein–protein interfaces that respond or are strengthened by transient increases in cellular zinc (reviewed in ref. 51). *S. cerevisiae* has been shown to possess millimolar amounts of zinc stored in the vacuole (52), which can be transported inside the cell via vesicular compartments (53). In the cell, zinc is tightly bound in metal–protein complexes with limited labile pools of exchangeable ions. However, the overall available concentration of zinc more than exceeds the K_d values measured in our study, suggesting it is plausible that transient increases in cellular zinc, or zinc release through reductive stress (54, 55), may play a physiological role in the Mec1-checkpoint.

Both Mec1 and Ddc2 are extensively phosphorylated in response to DNA damage, replication stress, and during the cell

cycle, in a Mec1-dependent and -independent manner, and are suggested to regulate the checkpoint (13, 24, 34, 56). Two characterized Ddc2 phosphosites, S173 and S182, have been shown to permanently arrest the cell cycle in response to a DSB when mutated to an alanine (13). Ddc2-S11 phosphorylation is suggested to be Cdk1-dependent *in vivo*, although S11 is not part of a canonical Cdk1 consensus motif (S/T-P-X-K/R, where X is any amino acid) (38). Cyclin dependent kinase (CDK) activity is required for double strand DNA break processing and checkpoint maintenance via Rad9 (ortholog of human 53BP1) phosphorylation (57), so it is possible that this phosphosite is indirectly modified by Cdk1 via its phosphorylation of another kinase that targets Ddc2. *In vitro* we find that S10 and S11 can be phosphorylated by CK2. However, we cannot rule out the activity of other acidophilic Ser/Thr kinases involved in Ddc2-phosphorylation, such as Dbf4-dependent Cdc7 kinase (DDK). Interestingly, similar to pS11 peptide, pS10 peptide also showed enhanced binding to Rfa1-NTD (Fig. 2F). However, unlike S11A, the S10A mutation did not show HU sensitivity (Fig. 2A). This further supports the idea that RPA dimerization induced by Ddc2 S11 phosphorylation plays major roles in Mec1–Ddc2 recruitment and DNA damage response. Possibly, S10 phosphorylation may be a priming phosphorylation event to stimulate S11 phosphorylation, analogous to Plk1/Cdc5 and CK2 phosphoregulation of human Rad51 (58). Indeed Plk1/Cdc5 and CK2 have both been implicated in the yeast DNA damage checkpoint (59). The exact kinase(s) responsible for phosphorylation of the Ddc2 N-terminal region will require more investigation but our study suggests that

ancillary kinases operate to enhance Mec1/ATR checkpoint kinase recruitment during replication (60).

Interestingly, in many other yeast species, including *K. lactis*, Asp replaces Ser in these equivalent positions, suggesting that the recruitment of Mec1–Ddc2 does not depend on Ddc2 phosphorylation in those species. An advantage of controlled oligomerization via phosphorylation is the ability to assemble complexes quickly with enhanced stability while being efficiently disassembled by dephosphorylation. While controlled/regulated oligomerization seems to be important for Mec1–Ddc2 recruitment in *S. cerevisiae*, this requirement might have been lost in other species. In humans, there is extensive phosphorylation of the N-terminal region of ATRIP; however, its role in ATR checkpoint function is not well understood. For example, CDK2 phosphorylation of S224 and S229 in human ATRIP, just outside the CC-domain, have been shown to regulate the DNA damage checkpoint (61), whereas two ATR-dependent sites within the RPA-interacting domain, S68 and S72, are suggested to be dispensable (62). Recent work suggests that ATRIP is acetylated at K32, which inhibits recruitment of ATR–ATRIP to RPA–ssDNA (63). ATRIP deacetylation by SIRT2 potentiates the ATR checkpoint and promotes ATR accumulation at ssDNA, RPA-binding, and enhances ATR–autophosphorylation (63). In this context, there is a possibility that ATRIP–RPA interactions are regulated by phosphorylation but have been masked by acetylation. The interplay between ATRIP acetylation and phosphorylation and its effect on recruitment to RPA–ssDNA will need to be investigated further.

Materials and Methods

Yeast Strains, Plasmids, and Proteins. Yeast strains used in this study were prepared as previously described (11). In brief, PY434 (*MAT α ade2-1 can1-100 his3-11,15 leu2-3,112 trp1-1 ura3-1 ddc2 Δ ::KANMX* containing pBL911 (pRS316, *URA3 DDC2*) was derived by genomic integration from C10-2A (*W303 RAD5 SML1*). Integration of *tel1 Δ ::NAT* in PY434 yielded PY436, and further integration of a *ddc1 Δ ::HIS3* cassette yielded strain PY437. The complementing plasmid pBL911 contains the *DDC2* gene on a centromeric plasmid under control of its own promoter, with *URA3* as both selectable and counter selectable (on 5-fluoroorotic acid, 5FOA) marker. Transformants were selected on Yeast extract peptone dextrose adenine (YPDA) plates containing the respective drug and verified by PCR analysis. We then generated a centromere plasmid for each of the Ddc2 mutants *p(ddc2-x LEU2)* pBL912-x (pRS315, *ddc2-x LEU2*) for genetic analysis, and a 2-micron plasmid pBL904-x (pRS424, 2 μ m ori *TRP1 MEC1 ddc2-x*) under control of the galactose-inducible *GAL1-10* promoter for overproduction of the Mec1–Ddc2-x complexes in yeast. All plasmids were verified by DNA sequencing. Detailed methods for DNA constructs used for recombinant protein expression is provided in *SI Appendix, Supplementary Methods*.

Purification of Proteins and Peptides. Strain PY439 (*MAT α can1 his3 leu2 trp1 ura3 GAL pep4 Δ ::HIS3 nam7 Δ ::KANMX4 ddc2 Δ ::KANMX6 sml1 Δ ::HYG*) was used to overexpress Mec1–Ddc2 or Mec1–ddc2-x mutants from the plasmid pBL904-x series, essentially as described previously (11). Detailed methods for protein production and purification, and a list of synthetic peptides used in this study are provided in *SI Appendix, Supplementary Methods*.

Kinase Assay. The kinase activity of Mec1–Ddc2 or Mec1–Ddc2-x complex was assessed as described previously (11) using the kinase-dead version (K227A) of Rad53, fused to the Glutathione-S-transferase (GST) purification tag (GST–Rad53-kd), as a probe. The assay was performed in 10 μ L 25 mM HEPES–NaOH pH 7.4, 2 % glycerol, 1 mM dithiothreitol (DTT), 20 μ g/mL bovine serum albumin (BSA), 0.08 % ampholytes pH 3.5 to 10, 8 mM Mg-acetate, 100 μ M adenosine triphosphate (ATP), 0.5 μ Ci [γ -³²P]ATP and 100 mM NaCl, and Dpb11 activator as indicated.

Yeast Cell Growth and Analysis. Yeast strains PY434, PY436, and PY437 were transformed with plasmid pBL912 or its derivatives and selected on SC–Ura–Leu plates using standard yeast growth media. Transformants were grown overnight in SC–Leu medium and plated on SC–Leu plates containing 5-fluoroorotic acid (5FOA) to allow growth only of cells that had lost plasmid

pBL911 (*URA3 DDC2*). These strains were grown in SC–Leu overnight at 30 °C and 10-fold serial dilutions spotted onto YPDA plates, with or without HU for varying times as indicated.

MST. MST experiments were performed using a Monolith NT.115 instrument (NanoTemper Technologies). In all cases premium-treated capillaries were used and the experiment conducted at 25 °C. Binding data were analyzed using NanoTemper Analysis 1.2.101 software and plotted in GraphPad Prism. Each experiment was technically repeated at least three or more times, and the mean half-effective concentration (EC₅₀), or K_d, values were calculated with SE using the law of mass action equation. Specific methods are given in *SI Appendix, Supplementary Methods*.

Gel Filtration Analysis. Rfa1-NTD in complex with near equimolar amounts of either Ddc2-peptide or pS11 Ddc2-peptide (200- μ L samples) were injected at a concentration of 10 mg/mL onto a Superdex S75 (10/300, Cytiva) in 25 mM 4-(2-Hydroxyethyl)piperazine-1-ethanesulfonic acid (HEPES), pH 7.0, 100 mM NaCl, with ZnCl₂ at indicated concentrations, at 25 °C, with a flow rate of 0.4 mL/min. The gel filtration column was equilibrated in the appropriate buffer between runs.

ITC. ITC measurements were performed on a MicroCal PEAQ-ITC calorimeter (Malvern Panalytical). Data were analyzed using the MicroCal PEAQ-ITC analysis software supplied by the manufacturer using the One Set of Sites model. Titrations were carried out at 750 rpm and at 25 °C. For each titration, the heat change associated with ligand dilution was measured and subtracted from the raw data. Specific methods are given in *SI Appendix, Supplementary Methods*.

Crystallization and Structure Determination. Rfa1-NTD in complex with pS11-Ddc2 peptide (⁴ETVGEFS[pS]DDDDDDILLELGT²⁴, where [pS] refers to a phosphoserine) was crystallized in; 10 mM zinc chloride, 0.1M 2-morpholinoethanesulfonic acid pH 6.0, 20% w/v polyethylene glycol (PEG) 6000 at 22 °C using nanoliter sitting drop vapor diffusion. Rfa1-NTD was also crystallized alone in 0.2 M lithium chloride, 0.1 M sodium acetate, pH 5.0, 20% (w/v) PEG 6000. Crystals were cryoprotected by the addition of ethylene glycol to a maximum concentration of 25% (v/v) before mounting and flash-freezing in liquid nitrogen. Diffraction revealed two crystal forms of space groups *P6₅22*, for the phosphopeptide complex, and *P2₁*, for Rfa1-NTD alone, resulting in two complete datasets with resolutions of 1.58 and 1.55 Å for the *P6₅22* and *P2₁* crystal forms, respectively. The crystal structures were determined by molecular replacement using Phaser (PDB 5OMB) and refined in the PHENIX package. Detailed methods for structure determination and refinement are given in *SI Appendix, Supplementary Methods*.

NSEM. Mec1–Ddc2 complexes expressed and purified essentially as described (11), were treated with 100 nM recombinant CK2 and 1 mM ATP with 4 mM Mg(OAc)₂ for 1 h at room temperature. The sample was diluted to ~170 nM, and equimolar amounts of Rfa1-NTD were added. The sample was split in half, and ZnCl₂ was added (100 μ M final concentration), or buffer without zinc. From each sample, 4 μ L was applied to freshly glow-discharged carbon-coated grids and incubated for 1 min. The excess sample was blotted, and two 4- μ L washes of distilled water were applied. The sample was stained by applying 4 μ L 2% (w/v) filtered uranyl acetate for 30 s and the excess blotted and allowed to air dry. Grids were imaged on a FEI (field electron and ion company) Tecnai G2 spirit 120 kV electron microscope equipped with a 2K camera at a nominal magnification of 67k, resulting in a pixel size of 3.5 Å. All images were collected manually with a defocus range from –2.5 to –3.5 μ m. Detailed methods for image analysis are given in *SI Appendix, Supplementary Methods*.

Data, Materials, and Software Availability. Crystal structure data have been deposited in PDB (8B4J (64) and 8B4K (65)).

ACKNOWLEDGMENTS. X-ray data collection was done at Diamond Light Source (Oxfordshire, UK). We thank Diamond for beamtime (proposal mx23620) and the staff of beamline 104. We thank the Centre of Structural Biology for crystallization and electron microscopy support. We thank Dr. L. Masino and the biophysics technology platform (Francis Crick Institute), for their support with isothermal titration calorimetry data, and Zhang and Burgers laboratory members for helpful discussions. This work was funded in part by Wellcome Trust grant no. 210658/Z/18/Z (to X.Z.) and by grant no. GM118129 from the NIH (to P.M.B.).

1. R. Kato, H. Ogawa, An essential gene, ESR1, is required for mitotic cell growth, DNA repair and meiotic recombination in *Saccharomyces cerevisiae*. *Nucleic Acids Res.* **22**, 3104–3112 (1994).
2. T. A. Weinert, G. L. Kiser, L. H. Hartwell, Mitotic checkpoint genes in budding yeast and the dependence of mitosis on DNA replication and repair. *Genes Dev.* **8**, 652–665 (1994).
3. E. J. Brown, D. Baltimore, ATR disruption leads to chromosomal fragmentation and early embryonic lethality. *Genes Dev.* **14**, 397–402 (2000).
4. Q. Liu *et al.*, Chk1 is an essential kinase that is regulated by Atr and required for the G(2)/M DNA damage checkpoint. *Genes Dev.* **14**, 1448–1459 (2000).
5. A. M. Casper, P. Nghiem, M. F. Arlt, T. W. Glover, ATR regulates fragile site stability. *Cell* **111**, 779–789 (2002).
6. R. Buisson, J. L. Boisvert, C. H. Benes, L. Zou, Distinct but Concerted Roles of ATR, DNA-PK, and Chk1 in Countering Replication Stress during S Phase. *Mol. Cell* **59**, 1011–1024 (2015).
7. M. O'Driscoll, V. L. Ruiz-Perez, C. G. Woods, P. A. Jeggo, J. A. Goodship, A splicing mutation affecting expression of ataxia-telangiectasia and Rad3-related protein (ATR) results in Seckel syndrome. *Nat. Genet.* **33**, 497–501 (2003).
8. M. S. Wold, Replication protein A: A heterotrimeric, single-stranded DNA-binding protein required for eukaryotic DNA metabolism. *Annu. Rev. Biochem.* **66**, 61–92 (1997).
9. L. Zou, S. J. Elledge, Sensing DNA damage through ATRIP recognition of RPA-ssDNA complexes. *Science* **300**, 1542–1548 (2003).
10. E. A. Tannous, P. M. Burgers, Novel insights into the mechanism of cell cycle kinases Mec1(ATR) and Tel1(ATM). *Crit. Rev. Biochem. Mol. Biol.* **56**, 441–454 (2021).
11. E. A. Tannous, L. A. Yates, X. Zhang, P. M. Burgers, Mechanism of auto-inhibition and activation of Mec1ATR checkpoint kinase. *Nat. Struct. Mol. Biol.* **28**, 50–61 (2021).
12. J.-C. Dubois *et al.*, A phosphorylation-and-ubiquitylation circuitry driving ATR activation and homologous recombination. *Nucleic Acids Res.* **45**, 8859–8872 (2017).
13. G. Memisoglu *et al.*, Mec1atr autophosphorylation and ddc2atrph phosphorylation regulates DNA damage checkpoint signaling. *Cell Rep.* **28**, 1090–1102.e3 (2019).
14. A. Maréchal *et al.*, PRP19 transforms into a sensor of RPA-ssDNA after DNA damage and drives ATR activation via a ubiquitin-mediated circuitry. *Mol. Cell* **53**, 235–246 (2014).
15. V. Hurst *et al.*, A regulatory phosphorylation site on Mec1 controls chromatin occupancy of RNA polymerases during replication stress. *EMBO J.* **40**, e108439. (2021).
16. E. J. Sanford *et al.*, Phosphoproteomics reveals a distinctive Mec1/ATR signaling response upon DNA end hyper-resection. *EMBO J.* **40**, e104566. (2021).
17. S. C. S. Bantele, M. Lisby, B. Pfander, Quantitative sensing and signalling of single-stranded DNA during the DNA damage response. *Nat. Commun.* **10**, 944 (2019).
18. S. J. Haring, A. C. Mason, S. K. Binz, M. S. Wold, Cellular functions of human RPA1. Multiple roles of domains in replication, repair, and checkpoints. *J. Biol. Chem.* **283**, 19095–19111 (2008).
19. H. L. Ball *et al.*, Function of a conserved checkpoint recruitment domain in ATRIP proteins. *Mol. Cell Biol.* **27**, 3367–3377 (2007).
20. J.-H. Choi *et al.*, Reconstitution of RPA-covered single-stranded DNA-activated ATR-Chk1 signaling. *Proc. Natl. Acad. Sci. U.S.A.* **107**, 13660–13665 (2010).
21. I. Deshpande *et al.*, Structural Basis of Mec1-Ddc2-RPA Assembly and Activation on Single-Stranded DNA at Sites of Damage. *Mol. Cell* **68**, 431–445.e5 (2017).
22. G. G. Oakley, S. M. Patrick, Replication protein A: Directing traffic at the intersection of replication and repair. *Front Biosci (Landmark Ed)* **15**, 883–900 (2010).
23. L. A. Yates *et al.*, A structural and dynamic model for the assembly of Replication Protein A on single-stranded DNA. *Nat. Commun.* **9**, 5447 (2018).
24. F. M. Bastos de Oliveira *et al.*, Phosphoproteomics reveals distinct modes of Mec1/ATR signaling during DNA replication. *Mol. Cell* **57**, 1124–1132 (2015).
25. S. Kumaran, A. G. Kozlov, T. M. Lohma, *Saccharomyces cerevisiae* replication protein A binds to single-stranded DNA in multiple salt-dependent modes. *Biochemistry* **45**, 11958–11973 (2006).
26. J. Rouse, S. P. Jackson, Lcd1p recruits Mec1p to DNA lesions in vitro and in vivo. *Mol. Cell* **9**, 857–869 (2002).
27. K. Kubrara, H. van Attikum, F. Hediger, S. M. Gasser, The processing of double-strand breaks and binding of single-strand-binding proteins RPA and Rad51 modulate the formation of ATR-kinase foci in yeast. *J. Cell Sci.* **120**, 4209–4220 (2007).
28. N. Dhingra *et al.*, The Srs2 helicase dampens DNA damage checkpoint by recycling RPA from chromatin. *Proc. Natl. Acad. Sci. U.S.A.* **118** (2021).
29. X. Wang *et al.*, 3.9 Å structure of the yeast Mec1-Ddc2 complex, a homolog of human ATR-ATRIP. *Science* **358**, 1206–1209 (2017).
30. H.-S. Kim, S. J. Brill, MEC1-dependent phosphorylation of yeast RPA1 in vitro. *DNA Repair (Amst)* **2**, 1321–1335 (2003).
31. C. A. Brosey *et al.*, Functional dynamics in replication protein A DNA binding and protein recruitment domains. *Structure* **23**, 1028–1038 (2015).
32. P. M. J. Burgers, Polymerase dynamics at the eukaryotic DNA replication fork. *J. Biol. Chem.* **284**, 4041–4045 (2009).
33. C. Xue *et al.*, Bloom helicase mediates formation of large single-stranded DNA loops during DNA end processing. *Nat. Commun.* **13**, 2248 (2022).
34. N. Hustedt *et al.*, Yeast PP4 interacts with ATR homolog Ddc2-Mec1 and regulates checkpoint signaling. *Mol. Cell* **57**, 273–289 (2015).
35. S. Lee, J. Heo, C.-J. Park, Determinants of replication protein A subunit interactions revealed using a phosphomimetic peptide. *J. Biol. Chem.* **295**, 18449–18458 (2020).
36. M. C. Lanz *et al.*, In-depth and 3-dimensional exploration of the budding yeast phosphoproteome. *EMBO Rep.* **22**, e51121. (2021).
37. C. P. Albuquerque *et al.*, A multidimensional chromatography technology for in-depth phosphoproteome analysis. *Mol. Cell Proteomics* **7**, 1389–1396 (2008).
38. L. J. Holt *et al.*, Global analysis of Cdk1 substrate phosphorylation sites provides insights into evolution. *Science* **325**, 1682–1686 (2009).
39. C. Zhou *et al.*, Profiling DNA damage-induced phosphorylation in budding yeast reveals diverse signaling networks. *Proc. Natl. Acad. Sci. U.S.A.* **113**, E3667–E3675 (2016).
40. A. Miller *et al.*, Zn-Enhanced Asp-Rich Antimicrobial Peptides: N-Terminal Coordination by Zn(II) and Cu(II), Which Distinguishes Cu(II) Binding to Different Peptides. *Int. J. Mol. Sci.* **22** (2021).
41. H. Zheng *et al.*, CheckMyMetal: A macromolecular metal-binding validation tool. *Acta Crystallogr. D Struct. Biol.* **73**, 223–233 (2017).
42. M. Laitaja, J. Valjakk, J. Jänis, Zinc coordination spheres in protein structures. *Inorg Chem.* **52**, 10983–10991 (2013).
43. E. Krissinel, K. Henrick, Inference of macromolecular assemblies from crystalline state. *J. Mol. Biol.* **372**, 774–797 (2007).
44. N. Nakazawa, O. Arakawa, M. Ebe, M. Yanagida, Casein kinase II-dependent phosphorylation of DNA topoisomerase II suppresses the effect of a catalytic topo II inhibitor, ICRF-193, in fission yeast. *J. Biol. Chem.* **294**, 3772–3782 (2019).
45. M. Sawicka *et al.*, The dimeric architecture of checkpoint kinases mec1atr and tel1atm reveal a common structural organization. *J. Biol. Chem.* **291**, 13436–13447 (2016).
46. J. Jumper, D. Hassabis, Protein structure predictions to atomic accuracy with AlphaFold. *Nat. Methods* **19**, 11–12 (2022).
47. M. Mirdita *et al.*, ColabFold: Making protein folding accessible to all. *Nat. Methods* **19**, 679–682 (2022).
48. S. Chen *et al.*, Structural basis of long-range to short-range synaptic transition in NHEJ. *Nature* **593**, 294–298 (2021).
49. Y. Yin *et al.*, A basal-level activity of ATR links replication fork surveillance and stress response. *Mol. Cell* **81**, 4243–4257.e6 (2021).
50. D. Menolfi *et al.*, Kinase-dead ATR differs from ATR loss by limiting the dynamic exchange of ATR and RPA. *Nat. Commun.* **9**, 5351 (2018).
51. A. Kocyla, J. B. Tran, A. Krężel, Galvanization of Protein-Protein Interactions in a Dynamic Zinc Interactome. *Trends Biochem. Sci.* **46**, 64–79 (2021).
52. C. Simm *et al.*, *Saccharomyces cerevisiae* vacuole in zinc storage and intracellular zinc distribution. *Eukaryotic Cell* **6**, 1166–1177 (2007).
53. C. Devirgiliis, C. Murgia, G. Danscher, G. Perozzi, Exchangeable zinc ions transiently accumulate in a vesicular compartment in the yeast *Saccharomyces cerevisiae*. *Biochem. Biophys. Res. Commun.* **323**, 58–64 (2004).
54. L. Li *et al.*, Metabolic remodeling maintains a reducing environment for rapid activation of the yeast DNA replication checkpoint. *EMBO J.* **41**, e108290. (2022).
55. A. G. Manford *et al.*, Structural basis and regulation of the reductive stress response. *Cell* **184**, 5375–5390.e16 (2021).
56. V. Paciotti, M. Clerici, G. Lucchini, M. P. Longhese, The checkpoint protein Ddc2, functionally related to *S. pombe* Rad26, interacts with Mec1 and is regulated by Mec1-dependent phosphorylation in budding yeast. *Genes Dev.* **14**, 2046–2059 (2000).
57. C. Y. Bonilla, J. A. Melo, D. P. Toczyski, Colocalization of sensors is sufficient to activate the DNA damage checkpoint in the absence of damage. *Mol. Cell* **30**, 267–276 (2008).
58. K. Yata *et al.*, Plk1 and CK2 act in concert to regulate Rad51 during DNA double strand break repair. *Mol. Cell* **45**, 371–383 (2012).
59. D. P. Toczyski, D. J. Galgoczy, L. H. Hartwell, CDC5 and CKII control adaptation to the yeast DNA damage checkpoint. *Cell* **90**, 1097–1106 (1997).
60. D. E. Hanna, A. Rethinaswamy, C. V. Glover, Casein kinase II is required for cell cycle progression during G1 and G2/M in *Saccharomyces cerevisiae*. *J. Biol. Chem.* **270**, 25905–25914 (1995).
61. J. S. Myers, R. Zhao, X. Xu, A.-J. L. Ham, D. Cortez, Cyclin-dependent kinase 2 dependent phosphorylation of ATRIP regulates the G2-M checkpoint response to DNA damage. *Cancer Res.* **67**, 6685–6690 (2007).
62. E. Itakura *et al.*, ATR-dependent phosphorylation of ATRIP in response to genotoxic stress. *Biochem. Biophys. Res. Commun.* **323**, 1197–1202 (2004).
63. H. Zhang *et al.*, ATRIP Deacetylation by SIRT2 Drives ATR Checkpoint Activation by Promoting Binding to RPA-ssDNA. *Cell Rep.* **14**, 1435–1447 (2016).
64. L. A. Yates, X. Zhang, PDB ID 8B4J, *Worldwide Protein Data Bank (wwPDB)*, <https://doi.org/10.2210/pdb8B4J/pdb>. Deposited 28 September 2022.
65. L. A. Yates, X. Zhang, PDB ID 8B4K, *Worldwide Protein Data Bank (wwPDB)*, <https://doi.org/10.2210/pdb8B4K/pdb>. Deposited 28 September 2022.